The Astrophysical Journal, 836:221 (13pp), 2017 February 20 https://doi.org/10.3847/1538-4357/836/2/221

The Planetary Accretion Shock. I. Framework for Radiation-hydrodynamical Simulations and First Results

Gabriel-Dominique Marleau[1,2], Hubert Klahr[2], Rolf Kuiper[3], and Christoph Mordasini[1]
[1] Physikalisches Institut, Universität Bern, Sidlerstr. 5, 3012 Bern, Switzerland; gabriel.marleau@space.unibe.ch
[2] Max-Planck-Institut für Astronomie, Königstuhl 17, D-69117 Heidelberg, Germany
[3] Institute for Astronomy and Astrophysics, Eberhard Karls Universität Tübingen, Auf der Morgenstelle 10, D-72076 Tübingen, Germany
Received 2016 August 30; revised 2016 December 27; accepted 2017 January 10; published 2017 February 22

Abstract

The key aspect determining the postformation luminosity of gas giants has long been considered to be the energetics of the accretion shock at the surface of the planet. We use one-dimensional radiation-hydrodynamical simulations to study the radiative loss efficiency and to obtain postshock temperatures and pressures and thus entropies. The efficiency is defined as the fraction of the total incoming energy flux that escapes the system (roughly the Hill sphere), taking into account the energy recycling that occurs ahead of the shock in a radiative precursor. We focus in this paper on a constant equation of state (EOS) to isolate the shock physics but use constant and tabulated opacities. While robust quantitative results will have to await a self-consistent treatment including hydrogen dissociation and ionization, the results presented here show the correct qualitative behavior and can be understood from semianalytical calculations. The shock is found to be isothermal and supercritical for a range of conditions relevant to the core accretion formation scenario (CA), with Mach numbers $\mathcal{M} \gtrsim 3$. Across the shock, the entropy decreases significantly by a few times k_B/baryon. While nearly 100% of the incoming kinetic energy is converted to radiation locally, the efficiencies are found to be as low as roughly 40%, implying that a significant fraction of the total accretion energy is brought into the planet. However, for realistic parameter combinations in the CA scenario, we find that a nonzero fraction of the luminosity always escapes the Hill sphere. This luminosity could explain, at least in part, recent observations in the young LkCa 15 and HD 100546 systems.

Key words: planets and satellites: formation – planets and satellites: gaseous planets – planets and satellites: physical evolution

1. Introduction

Starting with the discovery of planetary and low-mass companions to 2M 1207, 1RXS 1609, HR 8799, and β Pic in the last decade (Chauvin et al. 2004; Lafrenière et al. 2008; Marois et al. 2008; Lagrange et al. 2009), photometric and spectroscopic direct observations of several dozen young ($\lesssim$20–100 Myr old) objects have challenged and enriched our knowledge about exoplanets, providing access to their thermodynamic state, chemically complex atmospheres, and otherwise unobtainable information on the outer ($\gtrsim$20 au) architecture of planetary systems. One major limitation, however, has been the difficulty of determining the masses of these objects, which is of particular importance in light of recent or upcoming surveys expected to detect several young objects (e.g., LEECH, SPHERE, GPI, Project 1640, CHARIS; see Beuzit et al. 2008; Oppenheimer et al. 2012; Peters-Limbach et al. 2013; Macintosh et al. 2014; Skemer et al. 2014; G. Chauvin et al. 2017, in preparation; see also the review in Bowler 2016) as they seek to provide constraints on the mass distribution of planetary or very-low-mass companions (e.g., Biller et al. 2013; Brandt et al. 2014; Clanton & Gaudi 2016).

While the uncertainty on the age of the parent star often remains considerable, it is, to first order, presumably random. However, the conversion of a luminosity to a mass entails a theoretical, probably systematic uncertainty: that of the luminosity of a planet or low-mass object at the end of its formation, as it enters the evolutionary "cooling" phase.[4] This is a major source of uncertainty (Bowler 2016). Indeed, at those young ages, cooling has not yet erased traces of the formation process, as reflected in a planet's luminosity and radius (and thus also spectrum); this happens on the Kelvin–Helmholtz timescale $t_{KH} \equiv GM_p^2/RL \sim 10^7$–$10^9$ year. Formation models up to now (e.g., Marley et al. 2007; Mordasini et al. 2012a) have only made predictions in the limiting cases of "hot starts" and "cold starts," as discussed below, without however attempting to model the shock in detail.

What is thought to be the key process that sets the entropy of the gas is the accretion shock in the runaway gas accretion phase (Marley et al. 2007; Spiegel & Burrows 2012). This accretion shock is traditionally associated with core accretion, but it might also occur in some circumstances in the context of gravitational instability (see the discussion in Section 8.1 of Mordasini et al. 2012a). When the planet becomes massive enough, it detaches from the local disk (the "nebula"), and gas falls freely onto it. The question is usually put in terms of what happens to the kinetic energy of the gas, namely whether it is radiated away at the shock or whether it gets added as thermal energy to the planet. The extreme outcome of full radiative loss leads to "cold starts," while the limiting case of no radiative loss leads to "hot starts," as the resulting planets are then respectively colder or hotter (Marley et al. 2007).

Mordasini (2013) found that the mass of the solid core (in the core accretion framework) correlates with the postformation luminosity, but, as explained there, this is due to a self-amplifying process based on the shock. Thus the shock (or at least its computational treatment in formation calculations) is crucial in setting the postformation radius and luminosity.

[4] Deuterium burning might slow down the cooling, but the argument remains the same.

Marleau & Cumming (2014) have shown how to place joint constraints on the mass and initial entropy of an object from a luminosity and age measurement. Now, however, we take a first step toward predicting this initial entropy by presenting simulations of the shock efficiency, considering "snapshots" of the formation process.

In this first paper, we focus on the physics at the accretion shock and the upstream region. Since dissociation and ionization can act as energy sinks (Zel'dovich & Raizer 1967), we focus on an ideal gas equation of state (EOS) with constant heat capacity and mean molecular weight to isolate the shock physics from the microphysics. However, we use both constant and more realistic opacities. Also to simplify the analysis, we assume here that the gas and the radiation couple perfectly, and therefore we use "one-temperature" (1-T) radiation transport (discussed below). A forthcoming paper will be concerned with the effects of dissociation and ionization and will also address the importance of 2-T radiation transport. Finally, a subsequent work will also discuss how the shock results can be used in formation calculations and perform this coupling, following Berardo et al. (2017). Only with this will it be possible to predict directly postformation entropies and thus the luminosities and radii of young gas giants.

2. Model

2.1. Physical Picture

Each simulation is meant as a snapshot of the accretion process when the planet is at a radius $R_p = r_{shock}$, the shock radius. To follow gas accretion onto a growing planet that is detached from the nebula, we let our simulation box extend from the top-most layers of the planet to a large fraction of its accretion radius R_{acc}, defined through (Bodenheimer et al. 2000)

$$\frac{1}{R_{acc}} = \frac{1}{k_{Liss} R_{Hill}} + \frac{1}{R_{Bondi}}, \tag{1}$$

where

$$R_{Hill} = a\left(\frac{M_p}{3M_*}\right)^{1/3}, \quad R_{Bondi} = \frac{GM_p}{{c_\infty}^2} \tag{2}$$

are the Hill and Bondi radii, respectively, where a is the semimajor axis of the planet of mass M_p around a star of mass M_* and where c_∞ is the sound speed in the disk at the planet's location. The factor $k_{Liss} = 1/3$ accounts for the findings of Lissauer et al. (2009) that only the inner part of the material in the planet's Roche lobe is bound to it and most of the gas in the volume flows with the material in the disk (Mordasini et al. 2012a). The sphere of radius R_{acc} is thus the approximate region where gas should become bound to the planet, both in terms of gravitational force compared to that from the star (R_{Hill}) and thermal energy compared to the planet's potential energy (R_{Bondi}). In the runaway phase, the R_{Hill} term usually (though marginally) dominates (i.e., $R_{Hill} \lesssim R_{Bondi}$).

While global and local disk simulations have shown that the accretion onto the protoplanet is highly three-dimensional (Ayliffe & Bate 2009; Tanigawa et al. 2012; D'Angelo & Bodenheimer 2013; Fung et al. 2015; Ormel et al. 2015; Szulágyi et al. 2016) and possibly affected by magnetic fields in the gap and protoplanetary disk (e.g., Uribe et al. 2013; Keith & Wardle 2015), we take a first step here by using a spherically symmetric setup and neglecting magnetic fields. This allows us to model in detail the last stages of the accretion process on small scales around the protoplanetary object ($r \lesssim 30\,R_J$). These stages should remain similar in more complex geometries.

Note that, in the detached runaway phase, the continued accretion of solids (dust and planetesimals) by the planet is important for setting the final mass of the core (Mordasini 2013). However, this accretion rate of solids is several orders of magnitude smaller than that of gas and is therefore neglected here.

2.2. Methods

For our one-temperature radiation-hydrodynamics simulations, we use the static-grid version of the modular (magneto-) hydrodynamics code `PLUTO` (version 3; Mignone et al. 2007, 2012) combined with the gray, 1-T flux-limited diffusion (FLD) radiation transport module `Makemake` described and tested in Kuiper et al. (2010) and Kuiper & Klessen (2013), without ray tracing. We use the HLL hydrodynamical solver and the flux limiter λ from Levermore & Pomraning (1981) given by

$$\lambda(R) = \frac{2+R}{6+3R+R^2}, \tag{3}$$

where the radiation parameter R is defined through

$$F_{rad} = -D_F \nabla E_{rad}, \tag{4a}$$

$$D_F \equiv \frac{\lambda(R)c}{\kappa_R \rho}, \tag{4b}$$

$$R \equiv \frac{\|\nabla \ln E_{rad}\|}{\kappa_R\, \rho}, \tag{4c}$$

where F_{rad} and E_{rad} are the radiation flux and energy density, respectively, D_F is the Fick's law diffusion coefficient, κ_R is the Rosseland mean opacity, ρ is the density, and c is the speed of light. There is some freedom in the choice of the flux limiter's functional form, but it is required to behave asymptotically as (Levermore 1984)

$$\lambda(R) \to \begin{cases} \frac{1}{3}, & R \ll 1 \quad \text{(diffusion limit)} \\ \frac{1}{R}, & R \gg 1 \quad \text{(free-streaming limit)} \end{cases} \tag{5}$$

to recover the limiting regimes of pure diffusion, where $F_{rad} = \frac{1}{3} c \nabla E_{rad} / \kappa_R \rho$, and free streaming, where $F_{rad} = cE_{rad}$ in the direction opposite to the E_{rad} gradient.

The local radiation quantity $R(\rho, T, E_{rad})$ defined in Equation (4c) compares the photon mean free path $\lambda_{phot} = 1/\kappa\rho$ to the "radiation energy density scale height" $H_{E_{rad}} = E_{rad}/(\partial E_{rad}/\partial r)$ in spherical symmetry; in spherical coordinates it is thus given by

$$R = \frac{1}{\kappa \rho E_{rad}} \left| \frac{\partial E_{rad}}{\partial r} \right| = \left| \frac{\partial \ln E_{rad}}{\partial \tau} \right| \tag{6a}$$

$$= \frac{\lambda_{phot}}{H_{E_{rad}}}. \tag{6b}$$

Large R values mean that the radiation energy density—and thus, in the 1-T approximation, the gas temperature—changes over a shorter distance than photons get absorbed and reemitted.

2.3. Setup

We use a semiopen box fixed at some height in the atmosphere of the planet, with a closed left, inner edge (toward the center of the planet) at $r = r_{\rm min}$, and start with an atmosphere of some arbitrary small height (e.g., $0.5\,R_{\rm J}$), onto which gas falls from the outer edge of the grid at $r_{\rm max}$. For the initial setup, we calculate an atmosphere in hydrostatic equilibrium with a constant luminosity $L_{\rm p} = 10^{-3}\,L_{\odot}$ using the usual equations of stellar structure (but Equation (7d) as appropriate for an atmosphere):

$$\frac{dm_r}{dr} = 4\pi r^2 \rho, \tag{7a}$$

$$\frac{dT}{dr} = \nabla_{\rm act}\frac{T}{P}\frac{dP}{dr}, \tag{7b}$$

$$\frac{dP}{dr} = -\rho\frac{Gm_r}{r^2}, \tag{7c}$$

$$\frac{dL}{dr} = \frac{dm_r}{dr}\left(\varepsilon - T\frac{dS}{dr}\right), \quad = 0, \tag{7d}$$

where m_r is the mass interior to r (dominated by $M_{\rm p}$); P, T, and S are respectively the pressure, the temperature, and the entropy per mass; $L = 4\pi r^2 F_{\rm rad}$ is the luminosity; G is the universal gravitational constant; and ε is the energy-generation rate. The actual, adiabatic, and radiative gradients are given respectively by

$$\nabla_{\rm act} = \min(\nabla_{\rm ad}, \nabla_{\rm rad}) \tag{8a}$$

$$\nabla_{\rm ad} = \frac{\gamma - 1}{\gamma}, \tag{8b}$$

$$\nabla_{\rm rad} = \frac{3LP\kappa_{\rm R}}{64\pi\sigma G m_r T^4}. \tag{8c}$$

Equation (8a) is the Schwarzschild criterion. (Note that convection therefore plays a role only in the initial profile; in the radiation-hydrodynamical simulations proper, there is no convection because of the assumption of spherical symmetry.) We use an adaptive step size for the integration to resolve accurately the pressure and temperature gradients. This atmosphere is then smoothly joined onto a calculated accretion flow for ρ and v. (See Equations (11 and 12) below.) The goal of these efforts is to provide a numerically sufficiently smooth initial profile while beginning with a certain atmospheric mass to speed up the computation.

The grid is uniform from $r_{\rm min}$ to $r_{\rm min} + \Delta r$ and has a high resolution to resolve sufficiently well the pressure gradient in the innermost part, using by default $\Delta r = 0.5\,R_{\rm J}$ and $N = 500$ cells there. The other grid patch is a stretched segment out to $r_{\rm max}$, with usually also $N = 500$, and thus a much smaller resolution. This has proven to be stable and accurate.

As gas is added to the simulation domain, quasi-hydrostatic equilibrium is established below the shock. The shock position $r_{\rm shock}$ defining the top of the planet's atmosphere is simply given by the location where the gas pressure is equal to the ram pressure. The shock moves in time as gas is added (inward or outward depending on the simulation), usually at a negligible speed, that is, $dr_{\rm shock}/dt \ll v_{\rm shock}$, where $v_{\rm shock}$ is the preshock velocity. Nevertheless, we always take this term into account when calculating mass or energy fluxes; this possibly leads to slightly nonnominal effective accretion rates but allows for a more accurate verification of energy conservation. We consider only data from after an early adjustment phase, once the lab-frame accretion rate at the shock is equal to the one set through the outer boundary conditions, described below.

2.4. Boundary Conditions

For the hydrodynamics, reflective (zero-gradient) boundary conditions are used at $r_{\rm min}$ in the density, pressure, and velocity:

$$\frac{dP}{dr} = \frac{d\rho}{dr} = \frac{dv}{dr} = 0. \tag{9}$$

Since the condition $dv/dr = 0$ ensures that no mass flows over the boundary, it is not necessary to enforce hydrostatic equilibrium at $r_{\rm min}$. In the radiation transport also, we prevent the flow of energy over $r_{\rm min}$ by using

$$\frac{dE_{\rm rad}}{dr} = 0. \tag{10}$$

The outer edge of the grid $r_{\rm max}$ is set well outside the atmosphere and away from the shock. For the hydrodynamics, we choose an accretion rate and approximate the velocity as the free-fall velocity:

$$v(r) = v_{\rm ff}(r_{\rm max}) = \sqrt{2GM_{\rm p}\left(\frac{1}{r_{\rm max}} - \frac{1}{R_{\rm acc}}\right)}, \tag{11}$$

with $R_{\rm acc}$ defined in Equation (1). Mass conservation then determines the "free-fall density":

$$\rho_{\rm ff}(r_{\rm max}) = \frac{\dot{M}}{4\pi r^2 |v(r_{\rm max})|}. \tag{12}$$

The pressure gradient here too is required to vanish:

$$\left.\frac{dP}{dr}\right|_{r_{\rm max}} = 0. \tag{13}$$

We considered for some simulations a Dirichlet boundary condition with $P = P(\rho_{\rm ff}(r_{\rm max}), T_{\rm neb})$ for a nebula temperature $T_{\rm neb}$, taken as $T_{\rm neb} = 150$ K (e.g., Mizuno 1980). This did not change the results significantly.

Finally, the radiation outer boundary condition is usually set to the flux-divergence-free condition

$$\frac{\partial r^2 E_{\rm rad}}{\partial r} = 0, \tag{14}$$

which corresponds to a constant luminosity if the reduced flux $f_{\rm red}$, defined in Section 3.2, is sufficiently constant. Also, when the flux at the outer edge is in the diffusion regime, we obtain similar results for a Dirichlet boundary condition on the radiation temperature.

2.5. Microphysics

To isolate the shock physics, we consider in this work a constant EOS. The EOS enters into the radiation-hydrodynamical simulations through the effective heat capacity ratio $\gamma \equiv c_{\rm p}/c_{\rm v} =$

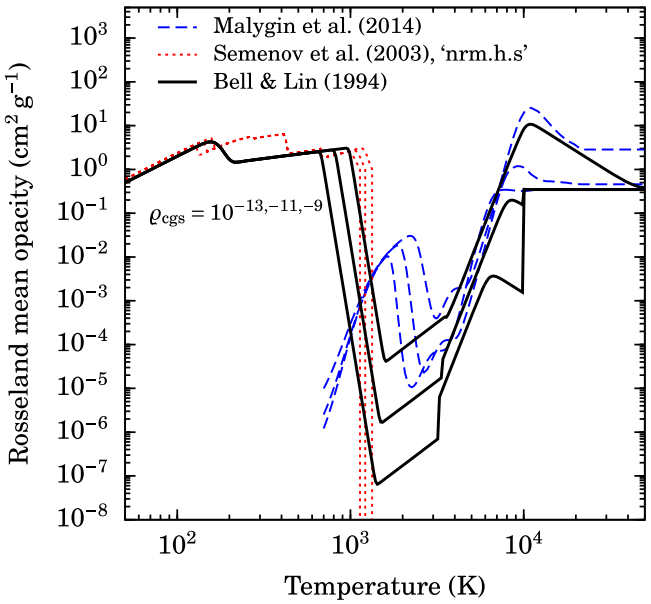

Figure 1. Gas, dust, and total Rosseland mean opacities from Malygin et al. (2014), Semenov et al. (2003), and Bell & Lin (1994). Three densities are shown: $\rho = 10^{-13,-11,-9}$ g cm^{-3}. For the Semenov et al. (2003) opacities, we use their "nrm.h.s" model, with dust grains made of "normal silicates" ([Fe/(Fe +Mg)] = 0.4) as homogeneous spheres. The Malygin et al. (2014) opacities are kept constant above the table limit of $T = 2 \times 10^4$ K.

$P/E_{\rm int} + 1$, where $E_{\rm int}$ is the internal energy per volume, and through the mean molecular weight μ. Estimates presented in the Appendix suggest that the hydrogen will be in molecular or atomic form at the shock. Since we consider a hydrogen–helium mixture with a helium mass fraction $Y = 0.25$, the combinations ($\mu = 2.343$, $Y = 1.44$), for the molecular hydrogen, and ($\mu = 1.23$, $\gamma = 1.1$), for atomic hydrogen, bracket the expected range (see Figure 4).

We consider both constant and tabulated opacities. The contribution of the dust to the opacity dominates below approximately 1400–1600 K, at which temperature the refractory components (olivine, silicates, pyroxene, and so on) evaporate (Pollack et al. 1994; Semenov et al. 2003). The standard opacity tables we use are the smoothed Bell & Lin (1994) fits. We can also make use of the Malygin et al. (2014) gas opacities combined with the dust opacities from Semenov et al. (2003) and compare these in Figure 1. Note that the Bell & Lin (1994) data lack water opacity lines just above the dust destruction temperatures (M. Malygin 2015, private communication; see also Figure 2 of Semenov et al. (2003) or Figure 1 of Arras & Bildsten 2006); as a consequence, their Rosseland opacities reach down to $\kappa_{\rm R} \sim 10^{-6}\,{\rm cm^2\,g^{-1}}$ for $\rho = 10^{-11}\,{\rm g\,cm^{-3}}$, some four orders of magnitude smaller than in more recent calculations (Freedman et al. 2008; Malygin et al. 2014).

Figure 4 shows that for low masses and accretion rates, the shock temperature should be $T_{\rm s} \lesssim 1500$ K, in which case the dust is not destroyed and the opacity is relatively high. When higher temperatures are reached, the opacity is lower by orders of magnitude, so the total (gas and dust) Rosseland opacities range from $\kappa_{\rm R} \sim 10^{-2}$ to $10\,{\rm cm^2\,g^{-1}}$ overall. This provides approximate values when considering constant opacities. Since 1-T FLD requires only the Rosseland mean, the subscript on $\kappa_{\rm R}$ will be dropped hereafter.

2.6. Quantities to Be Measured

2.6.1. Efficiencies

The main goal of this study is to determine the radiative loss efficiency of the accretion shock. There are several ways of defining this. The classical definition, $\eta^{\rm kin}$, indicates what fraction of the inward-directed kinetic energy flux is converted into a jump in outgoing radiative flux (e.g., Hartmann et al. 1997; Baraffe et al. 2012; Zhu 2015). This kinetic-energy luminosity is at most

$$L_{\rm acc,max} = 4\pi R_{\rm p}^2 \frac{1}{2}\rho v^3 = \frac{1}{2}\dot{M}v^2 \tag{15}$$

$$\approx \frac{GM_{\rm p}\dot{M}}{R_{\rm p}}, \tag{16}$$

where $\dot{M} = 4\pi r^2 \rho v$ is the mass accretion rate (neglecting the sign of v), and the last expression is valid for free fall from a large radius. Therefore, the energy actually radiated away at the shock is written as

$$L_{\rm acc} = \eta^{\rm kin}\frac{GM_{\rm p}\dot{M}}{R_{\rm p}}, \tag{17}$$

and it is usually assumed that $\eta^{\rm kin} = 100\%$ (i.e., full loss). This is called "cold accretion." Note that this $\eta^{\rm kin}$ corresponds to the quantity $(1 - \eta)$ of Spiegel & Burrows (2012), $\alpha_{\rm h}$ of Mordasini et al. (2012a), $(1 - \alpha)$ of Hartmann et al. (1997), and X of Commerçon et al. (2011).

We present here and use a second definition based on the total energy available. This efficiency $\eta^{\rm phys}$ measures what fraction of the total energy flowing toward the planet actually remains below the shock, that is, is absorbed by the embryo:

$$\eta^{\rm phys} \equiv \frac{\dot{E}(r_{\rm max}) - \dot{E}(r_{\rm shock}{}^-)}{\dot{E}(r_{\rm max})}, \tag{18}$$

where $r_{\rm shock}{}^-$ is immediately downstream of the shock, and the outer edge of the computation domain $r_{\rm max}$ is used as a proxy for the accretion radius $R_{\rm acc}$ corresponding to the location of the nebula. The material energy flow rate is defined as

$$\dot{E}(r) \equiv -|\dot{M}|[e_{\rm kin}(r) + h(r) + \Delta\Phi(r, r_{\rm shock})], \tag{19}$$

where $e_{\rm kin} = \frac{1}{2}v^2$, $e_{\rm int}$, and $h = e_{\rm int} + P/\rho$ are respectively the kinetic energy, internal energy density, and the enthalpy per unit mass, and Φ is the external potential. The $\Delta\Phi$ term in Equation (19) accounts for the work done by the potential on the gas down to the shock, with the potential difference from r_0 to r given by

$$\Delta\Phi(r, r_0) = -GM_{\rm p}\left(\frac{1}{r} - \frac{1}{r_0}\right). \tag{20}$$

Thus $\eta^{\rm phys}$ measures how much of the incoming energy flow $\dot{E}(r_{\rm max})$ in the gas is still flowing inward once it has passed through the shock; if both are equal ($\dot{E}(r_{\rm shock}{}^-) = \dot{E}(r_{\rm max})$), $\eta^{\rm phys} = 0$ and the accretion would be thought of as "hot." If in the other extreme case none of the energy traverses the shock, $\eta^{\rm phys} = 100\%$, implying that the energy must have been entirely converted to outward-traveling radiation. This therefore automatically reflects the fact that the (non)heating of the planet is determined by the *imbalance* between the amount of

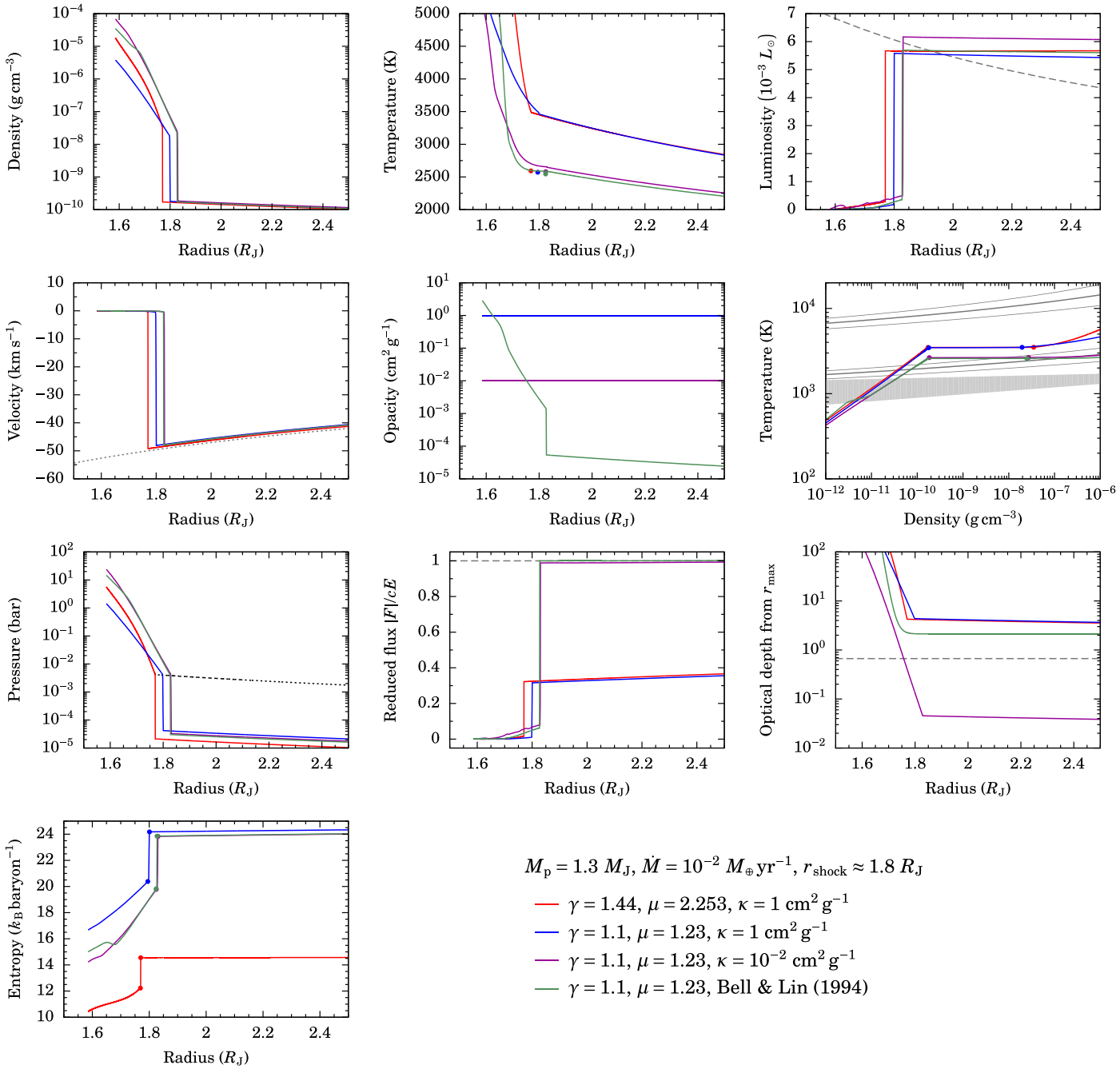

Figure 2. Detailed shock profiles for simulations with $M_p = 1.3\ M_J$, $r_{shock} \approx 1.8\ R_J$, and $\dot{M} = 10^{-2}\ M_\oplus\ \mathrm{yr}^{-1}$ using a constant equation of state and constant opacities or the Bell & Lin (1994) opacities (see legend). The simulation grids extend to 0.7 of the accretion radius $R_{acc} \approx 250\ R_J$, but only the inner region is shown. The axis labels describe the quantities shown, and only a few comments are needed, as follows. The temperature panel also shows the lower-bound estimate of Equation (28b) (solid dots). In the luminosity panel, the maximal accretion luminosity $L_{acc,max}(r) = 0.5\dot{M}v(r)^2 \approx GM_p\dot{M}/r$ is shown at every radius (the gray dashed curve). The velocity panel also displays the free-fall velocity from R_{acc} (the same for all simulations; the gray dotted line). In the opacity panel, simulations with constant opacity overlap. In the temperature–density phase diagram, the solid dots mark the up- and downstream conditions of shock; the solid lines show contours of 10%, 50% (thicker), and 90% atomic hydrogen (relative to the hydrogen species); and the gray region highlights where the dust is being destroyed, with $\kappa \sim 1\ \mathrm{cm}^2\ \mathrm{g}^{-1}$ below and $\kappa \sim 10^{-6}$–$10^{-3}\ \mathrm{cm}^2\ \mathrm{g}^{-1}$ above in the Bell & Lin (1994) opacities. The pressure panel also displays the ram pressure $P_{ram} = \rho v^2$, the same for all simulations (the dashed curve). The entropy is computed self-consistently from Equation (29a).

kinetic energy converted to internal energy and the reemitted radiation.

By energy conservation, the numerator of η^{phys} should be equal to the difference $\dot{E}(r_{shock}{}^+) - \dot{E}(r_{shock}{}^-)$ between the material energy flow rate directly across the shock. This is true for a zero-temperature gas (infinite Mach number), for which the potential energy is entirely converted into kinetic energy by the external potential. For finite temperatures, however, a (small) pressure gradient builds up ahead of the shock; in this case, only part of the change in potential energy serves to increase the kinetic energy, the remainder going into internal energy and thus, outside of phase transitions, into pressure.

Also by energy conservation, $\Delta\dot{E}(r_{\rm shock}{}^{\pm})$ measured in the shock frame should be equal (up to a sign) to the change in the luminosity ΔL across the shock. However, in the case that the radiative precursor (Zel'dovich & Raizer 1967) is contained within the accretion region—roughly the Hill sphere—it is not true anymore that $\dot{E}(r_{\rm shock}{}^{+}) = \dot{E}(r_{\rm max})$. In fact, the luminosity upstream of the precursor can be smaller than downstream (i.e., the planet is invisible, at least in the gray approximation), which would lead to a negative efficiency if using ΔL. Thus, $\Delta\dot{E}$ is a more useful numerator because it is intuitive and applicable both when the precursor reaches $r_{\rm max}$ and when it does not.

Note finally that the definition of Equation (18) takes into account the fact that even if the entire kinetic energy is converted to luminosity, the net efficiency can still be zero if this radiation is absorbed by the incoming material. This was seen by Vaytet et al. (2013a) in the case of Larson's second core and estimated by Baraffe et al. (2012) to be the case at high accretion rates in the context of magnetospheric accretion onto stars.

Thus, we will focus in this study on the efficiencies as defined above: on the classical, "kinetic" efficiency $\eta^{\rm kin}$, which makes a direct statement about the energy conversion at the shock, with $\eta^{\rm kin} < 100\%$ for either an isothermal shock at Mach number $\mathcal{M} \lesssim 2.5$ (Commerçon et al. 2011) or an nonisothermal shock; and on the "physical" efficiency $\eta^{\rm phys}$, which indicates how much the upstream gas is able to recycle the energy liberated at the shock (Drake 2006).

2.6.2. Postshock Entropy

The postshock temperature and thus entropy depend on the thermal profile of the layers below the shock, which are expected to adjust to carry the luminosity from deeper down (Paxton et al. 2013). Since however we do not attempt to predict this luminosity accurately with our setup of a truncated atmosphere, the reported temperature values will serve only as an indication. Moreover, there is a nontrivial relationship between the postshock entropy values and their influence on the entropy of the planet's deep adiabat; in particular, the postshock material does not simply set, weighted by mass, the interior entropy. This question is the subject of separate studies (Berardo et al. 2017; G.-D. Marleau et al. 2017, in preparation), which however require the obtained postshock entropies as boundary conditions.

3. Results: Radial Profiles and Efficiencies

We have performed a large number of simulations, varying physical parameters (mass, radius, accretion rate) but also computational or numerical settings (technique for accreting gas into the domain, outer temperature boundary condition, resolution, Courant number, and so on). For the latter, we select the most stable setup (as described in Section 2.2 above) and present results for a typical combination relevant to core accretion formation calculations (Bodenheimer et al. 2000; Mordasini et al. 2012a). We look at the properties of the accretion shock for $M_{\rm p} = 1.3\,M_{\rm J}$, $\dot{M} = 10^{-2}\,M_{\oplus}\,{\rm yr}^{-1}$, and $r_{\rm shock} \approx 1.8\,R_{\rm J}$. The Bondi, Hill, and resulting accretion radius according to Equation (1) are $R_{\rm Bondi} \approx 4200\,R_{\rm J}$, $R_{\rm Hill} \approx 800\,R_{\rm J}$, and $R_{\rm acc} \approx 250\,R_{\rm J}$ (for $T_{\rm neb} = 150$ K and a solar-mass star, which however does not affect $R_{\rm acc}$ strongly). Figure 2 shows the detailed structure of the accretion flow near the shock for $\kappa = 10^{-2}$ and $1\ {\rm cm}^2\,{\rm g}^{-1}$, as well as with the Bell & Lin (1994) opacities. The radial structures are as expected and show a number of typical features, which we discuss in the following.

3.1. Density, Velocity, and Pressure

The density and velocity reveal gas almost exactly free-falling onto a nearly hydrostatic atmosphere abruptly cut off at the shock. The mass in the total domain, dominated by the postshock region, is typically $\Delta M \sim 10^{-4}\,M_{\oplus}$, making perfectly justified the neglect of the self-gravity of the gas. The density jumps at the shock by a factor $\rho_2/\rho_1 \sim 200$, where ρ_2 and ρ_1 are the post- and preshock density. Thanks to the transport of energy by radiation, this is a much larger compression than the infinite Mach number limit for a hydrodynamical shock, where $\rho_2/\rho_1 = (\gamma+1)/(\gamma-1) \approx 4$ to 20 for $\gamma = 5/3$ to 1.1 (e.g., Mihalas & Mihalas 1984; Commerçon et al. 2011). As it falls deeper in the potential well of the planet, the gas slows down to slightly sub-free-fall speeds due to the pressure gradient caused by the increasing temperature and density.

The postshock pressure is given very accurately by the ram pressure of the incoming gas:

$$P_{\rm post} = P_{\rm ram} = \rho v^2. \tag{21}$$

This differs slightly from the strong-shock (high Mach number), nonradiating case where $P_{\rm post} = 2/(\gamma+1)\rho v^2$ (Drake 2006, his Equation (4.18)), as we verified with a simulation using a higher $\gamma = 5/3$ to increase the difference.

3.2. Optical Depth, Reduced Flux, and Radiation Regime

We begin by discussing the reduced flux. The reduced flux

$$f_{\rm red} \equiv F_{\rm rad}/(cE_{\rm rad}) \tag{22}$$

is a *local* measure of the extent to which radiation is streaming freely ($f_{\rm red} \to 1$) or diffusing ($f_{\rm red} \to 0$). This is thus the more correct, physical measure of what is often loosely termed the "optical depth," as discussed below. The reduced flux, radiation quantity R, and flux limiter λ are related in general by $f_{\rm red} = \lambda(R)R$. Note that the effective speed of propagation of the photons is $c_{\rm eff} = f_{\rm red}\,c$.

Next, we consider the optical depth. For a free-fall profile with $R_{\rm acc} \gg r_{\rm shock}$ (so that $\rho \propto r^{-3/2}$) and a radially sufficiently constant opacity ($\kappa \propto r^{\alpha}$ with $|\alpha| \ll 1/2$), the optical depth to the shock is

$$\Delta\tau = \int_{r_{\rm shock}}^{\infty} \kappa(r)\rho(r)dr \tag{23a}$$

$$= 2\kappa\rho r_{\rm shock} \qquad (\text{const. } \kappa), \tag{23b}$$

where $\kappa\rho$ is evaluated at the shock.[5] For the data of Figure 2, $\rho = 1.5\times10^{-10}\,{\rm g\,cm}^{-3}$ upstream of the shock, so that $\Delta\tau = 3.9\,(\kappa/1\ {\rm cm}^2\,{\rm g}^{-1})$. This agrees very well with the actual optical depths (measured from $r_{\rm max} = 0.7R_{\rm acc} \approx 175\,R_{\rm J}$) in the constant opacity cases. For the simulation with the Bell & Lin (1994) opacities, the estimate is moderately accurate, if one takes for κ not the actual preshock value ($\kappa \sim 10^{-5}\,{\rm cm}^2\,{\rm g}^{-1}$,

[5] This justifies (within a factor of a few) the estimate $\kappa\rho r_{\rm shock}$ of Stahler et al. (1980) for the optical depth upstream (and not downstream, as the formula might at first suggest) of the accretion shock in the context of Larson's second core. The estimate is certainly rough for a nonconstant opacity, but at least it does estimate the optical depth in the correct (upstream) direction. A similar expression is used by Mordasini et al. (2012a) in their boundary conditions.

set by the gas) but rather a typical value ($\kappa \sim 1\ \mathrm{cm^2\ g^{-1}}$) in the outer regions ($r \gtrsim 40\ R_\mathrm{J}$), where the dust is not destroyed. Also for nonconstant opacities, then, the optical depth to the shock will be roughly given by

$$\Delta\tau \sim 3\left(\frac{\kappa}{1\ \mathrm{cm^2\ g^{-1}}}\right)\left(\frac{\dot{M}}{10^{-2}\ M_\oplus\ \mathrm{yr^{-1}}}\right)\sqrt{\left(\frac{1\ M_\mathrm{J}}{M_\mathrm{p}}\right)\left(\frac{2\ R_\mathrm{J}}{r_\mathrm{shock}}\right)}, \tag{24}$$

using $\dot{M} = 4\pi r^2 \rho v$. Since the nebula should always be at temperatures lower than the dust destruction temperature $T_\mathrm{dest} \approx 1500\ \mathrm{K}$, the high opacity of the dust will always contribute to the optical depth. Therefore, independent of whether dust is destroyed in the inner parts of the flow, close to the shock, the opacity to insert in Equation (24) should be of order $\kappa \sim 1\ \mathrm{cm^2\ g^{-1}}$.

Second, in writing $E_\mathrm{rad} = F_\mathrm{rad}/(cf_\mathrm{red}) \propto L/(r^2 f_\mathrm{red})$, it is clear that when L/f_red is locally spatially constant ($L/f_\mathrm{red} \propto r^\beta$ with $|\beta| \ll 2$), the radiation quantity $R = 1/(\kappa\rho)|\partial \ln E_\mathrm{rad}/\partial r|$ is given by $R \approx 2/(\kappa\rho r)$, where $\kappa\rho$ and r are evaluated locally.[6] This result applies in general, independent of the radiation regime (diffusion or free streaming).

Combining these observations leads to the result that, in the case of constant opacity and L/f_red, the reduced flux upstream of the shock is

$$f_\mathrm{red}\left({r_\mathrm{shock}}^+\right) = \lambda\left(\frac{4}{\Delta\tau}\right) \times \frac{4}{\Delta\tau} \tag{25a}$$

$$\approx \left(\frac{3}{4}\Delta\tau + 1\right)^{-1}, \tag{25b}$$

where the second line would be an equality for the simple flux limiter $\lambda = 1/(3 + R)$ (LeBlanc & Wilson 1970; Levermore 1984; Ensman 1994). We will return to this result in Section 3.3. For a nonconstant opacity, Equation (25) provides in fact an approximate lower bound of $f_\mathrm{red}\left({r_\mathrm{shock}}^+\right)$ given $\Delta\tau$ or vice versa: indeed, a low opacity in front of the shock will drive down f_red (compared to the prediction of Equation (25)) but without decreasing much the total optical depth. This highlights the conceptual independence between the (nonlocal) optical depth and the (local) radiation transport regime (free streaming or diffusion).

The optical depths from the shock out to $r_\mathrm{max} \approx R_\mathrm{acc}$ are $\Delta\tau \approx 2$–5 for all except the $\kappa = 10^{-2}\ \mathrm{cm^2\ g^{-1}}$ simulation, which has $\Delta\tau \approx 3 \times 10^{-2}$. (A comparison run with the dust opacities of Semenov et al. (2003) and the gas opacities of Malygin et al. (2014) yielded very similar profiles and optical depths.) In the $\kappa \neq 10^{-2}\ \mathrm{cm^2\ g^{-1}}$ simulations, the shock would therefore be called "optically thick." However, the effective speed of light $c_\mathrm{eff} = f_\mathrm{red}\, c \gtrsim 0.3c$ throughout the flow (see below), which is still orders of magnitude larger than the gas flow speed $v \sim 10^{-4}c$. This is the regime Mihalas & Mihalas (1984) term "static diffusion." Therefore, the radiation is able to diffuse into the incoming gas, heating it up out to the edge of the computation grid, near the accretion radius. In other words, the shock precursor is larger than the Hill radius, which implies that the radiation should be able to escape from the system to at least the local disk. In this sense, the shock for these parameter values is an optically thick–thin shock (downstream and upstream, respectively) in the classification of Drake (2006). That, despite the somewhat high optical depth, the shock is not equivalent to a hydrodynamical shock is already hinted at by the large compression ratio pointed out in Section 3.1.

[6] It may seem surprising that the local quantity R depends on an absolute coordinate r, but this is in fact a simple consequence of the (spherical) geometry.

3.3. Temperature

3.3.1. Shock Temperature

For all choices of κ and the EOS (γ, μ), the temperatures immediately upstream and downstream of the shock are essentially equal; that is, there is no jump in the temperature. This is thus a *supercritical* shock (Zel'dovich & Raizer 1967), in which the downstream gas is able to preheat the incoming gas up to the postshock temperature. Note that the 1-T approach to the radiation transport used here cannot reveal the Zel'dovich spike expected in the gas temperature. This feature of radiation-hydrodynamical shocks consists of a sharp increase of the gas temperature immediately behind the shock, followed by a quick decrease in a "radiative relaxation region," while the radiation temperature remains essentially constant (Zel'dovich & Raizer 1967; Mihalas & Mihalas 1984; Stahler et al. 1980; see Drake 2007 and Vaytet et al. 2013b for a more detailed description). However, this is not of concern since this spike is very thin both spatially (physically, a few molecular mean free paths, broadened in simulations to a few grid cells; e.g., Ensman 1994; Vaytet et al. 2013b; G.-D. Marleau et al. 2017, in preparation) and in optical depth, and below the Zel'dovich spike, the matter and radiation equilibrate again. Therefore, the Zel'dovich spike should affect neither the postshock temperature or entropy nor the shock efficiency. A possible disequilibrium in temperatures just upstream of the shock will be explored in a forthcoming publication.

We find shock temperatures of $T_\mathrm{shock} \approx 2500\ \mathrm{K}$ for the cases with a low preshock opacity ($\kappa = 10^{-2}\ \mathrm{cm^2\ g^{-1}}$ or with Bell & Lin 1994), but $T_\mathrm{shock} \approx 3500\ \mathrm{K}$ for the other two cases, both with $\kappa = 1\ \mathrm{cm^2\ g^{-1}}$. These temperature values (and their relatively large difference of 1000 K) can be understood from an analytical estimate, presented next. First, one can always write

$$F\left({r_\mathrm{shock}}^+\right) = F\left({r_\mathrm{shock}}^-\right) + \eta^\mathrm{kin}\frac{1}{2}\rho {v_\mathrm{shock}}^3, \tag{26}$$

where ρ is the density just ahead of the shock, v_shock is the velocity at the same location, and η^kin is the "kinetic energy loss efficiency," discussed in Section 3.6. In general, the flux on either side of the flux is $F\left({r_\mathrm{shock}}^\pm\right) = f_\mathrm{red}^\pm caT^4\left({r_\mathrm{shock}}^\pm\right)$, where ${f_\mathrm{red}}^\pm \equiv f_\mathrm{red}\left({r_\mathrm{shock}}^\pm\right)$ and a is the radiation constant, related to the Stefan–Boltzmann constant σ by $ac = 4\sigma$. Note that here $f_\mathrm{red} = F_\mathrm{rad}/cE_\mathrm{rad}$ should be negative (one usually implicitly takes the norm) if the downstream radiation is flowing inward ($F_\mathrm{rad} < 0$). For an isothermal shock at T_shock, Equation (26) then implies that

$$\sigma {T_\mathrm{shock}}^4 = \frac{\eta^\mathrm{kin}}{4\Delta f_\mathrm{red}}\frac{\rho {v_\mathrm{shock}}^3}{2}, \tag{27}$$

where $\Delta f_{\rm red} \equiv {f_{\rm red}}^{+} - {f_{\rm red}}^{-}$. Combining with Equations (24) and (25) yields the estimates for an isothermal shock

$$T_{\rm shock}(\Delta\tau \ll 1) \approx 2315\ {\rm K} \left(\frac{r_{\rm shock}}{2\ R_{\rm J}}\right)^{-3/4} \times \left(\frac{\dot{M}}{10^{-2}\ M_{\oplus}\ {\rm yr}^{-1}}\right)^{1/4} \left(\frac{M}{1\ M_{\rm J}}\right)^{1/4} \quad (28a)$$

$$T_{\rm shock}(\Delta\tau \gg 1) \approx 2710\ {\rm K} \left(\frac{r_{\rm shock}}{2\ R_{\rm J}}\right)^{7/8} \left(\frac{\kappa}{1\ {\rm cm^2\ g^{-1}}}\right)^{1/4} \times \left(\frac{\dot{M}}{10^{-2}\ M_{\oplus}\ {\rm yr}^{-1}}\right)^{1/2} \left(\frac{M}{1\ M_{\rm J}}\right)^{1/8}, \quad (28b)$$

where a $(\eta^{\rm kin})^{1/4}$ factor was left out on the right-hand sides since we find it is ≈1 (see Section 3.6). The first expression used the fact that, by Equation (25), $\Delta\tau \ll 1$ implies ${f_{\rm red}}^{+} \approx 1$, and further took ${f_{\rm red}}^{-} \ll {f_{\rm red}}^{+}$. The second case is somewhat crude for nonconstant opacities. This assumes a constant luminosity in the shock's near upstream vicinity. Since the postshock region is very dense, ${f_{\rm red}}^{-}$ is small; this is equivalent to neglecting the downstream luminosity, which is related in a nontrivial way to the interior luminosity of the planet (Berardo et al. 2017; G.-D. Marleau et al. 2017, in preparation).

The solid circles in Figure 2 show the lower bound of Equation (28b). The simulations with a low preshock opacity ($\kappa = 10^{-2}\ {\rm cm^2\ g^{-1}}$ or with Bell & Lin 1994) have $f_{\rm red} \approx 1$ upstream of the shock and indeed have a temperature given by Equation (28b), whereas in the other cases a higher temperature is needed to carry a similar luminosity. The difference is quite large and nearly 1000 K. One way of thinking about this is that the effective speed of light is lower than c, so that $E_{\rm rad}$ must increase in order to reach the same $F_{\rm rad} = c_{\rm eff} E_{\rm rad}$.

Interestingly, the molecular and atomic hydrogen cases lead to a very similar temperature $T_{\rm shock} = 3500$ K. The phase diagram indicates that the atomic hydrogen simulation with $\kappa = 1\ {\rm cm^2\ g^{-1}}$ is self-consistent, but that the case with atomic hydrogen and detailed opacities leads to temperatures and densities where the dissociation process (and thus a varying μ and γ) would be important. One can already anticipate the result that, for an isothermal shock, the hydrogen should *recombine* in part through the shock (G.-D. Marleau et al. 2017, in preparation) since at fixed temperature the abundance of H_2 increases with density.

Note that Stahler et al. (1980, their Equation (24)) present an estimate similar to Equation (27) in the context of stellar accretion. Their assumptions about the reprocessing of shock photons[7] imply that, when $F_{\rm rad}({r_{\rm shock}}^{-}) \ll F_{\rm rad}({r_{\rm shock}}^{+})$ and neglecting their T_d term, $\Delta f_{\rm red} \approx {f_{\rm red}}^{+} \approx 1/3$ automatically. Commerçon et al. (2011, their Equations (22) or (53)) give a formula similar to Equation (27) in the limiting case $\eta^{\rm kin} = 1$ but do not include the factor $1/(4\Delta f_{\rm red})$. This is because they equate the temperature at the shock with the *effective* temperature needed to radiate away the kinetic energy, increasing the temperature estimate by ≈40% (a factor $4^{1/4} \approx 1.4$), or ≈1200 K for $T_{\rm s} \approx 3000$ K.

[7] They assume that half of the photons generated at the shock move inward and the other half outward; in turn, one-half of this outward-moving radiation is assumed to be reradiated inward by an absorbing layer ahead of the shock. If one ignores the contribution from the interior luminosity, this implies that $\eta^{\rm kin} = 25\%$. However, it seems to us that one needs radiative transfer calculations such as the ones presented here (or using more detailed radiation transport as in Drake 2007) to justify this accounting.

3.3.2. Temperature Profile

Equation (22) implies that, if the luminosity and the reduced flux are radially roughly constant, $T \propto r^{-1/2}$ since $L = 4\pi r^2 F_{\rm rad}$, independent of the optical depth to the shock. This is the case for the constant-κ simulations but not so for the tabulated opacities (at larger radial distances than shown).

Note that if the temperature increased solely due to adiabatic compression, that is, at constant entropy in the absence of radiation transport, we would have $T \propto \rho^{\gamma-1} \propto r^{-1.5(\gamma-1)}$, that is, $T \propto r^{-0.15}$ or $T \propto r^{-0.66}$ for $\gamma = 1.1$ or 1.44, respectively. Thus, when $T \propto r^{-1/2}$, entropy decreases inward if $\gamma > 4/3 \approx 1.33$.

3.4. Entropy

To compute the entropy, we use the Sackur–Tetrode equation (e.g., Marleau & Cumming 2014; Berardo et al. 2017, and references therein) for an ideal gas composed of H_2 and He or H and He:

$$S_{\rm H_2\text{-}He} = 8.80 + 3.38 \log_{10}\left(\frac{T}{1000\ {\rm K}}\right) - 1.01 \log_{10}\left(\frac{P}{1\ {\rm bar}}\right), \quad (29a)$$

$$S_{\rm H\text{-}He} = 13.47 + 4.68 \log_{10}\left(\frac{T}{1000\ {\rm K}}\right) - 1.87 \log_{10}\left(\frac{P}{1\ {\rm bar}}\right), \quad (29b)$$

respectively, using $Y = 0.243$, and where the entropies are in units of Boltzmann's constant per baryon, $k_{\rm B}$/baryon. In Figure 2, we see that the entropy *decreases* across the shock by $|\Delta S| \approx 2.5$ and 4.0 $k_{\rm B}$/baryon for the molecular and atomic cases, respectively. (In general but for constant γ and μ, the jump in entropy at an isothermal shock is $\Delta S = -2.303/\mu \times \log_{10}(\gamma \mathcal{M}^2)$ in units of $k_{\rm B}$/baryon.) The fact that the entropy decreases through this shock is actually in agreement with the statement that entropy increases across a hydrodynamical shock. Indeed, once it arrives at the radiative shock found here, the gas has already seen its entropy increase from the value far outside the precursor. (In the case that the precursor is larger than the simulation domain, as applies for these simulations, this "far-field" value cannot be obtained directly. However, already at $r_{\rm max}$ the entropy is much lower than it is downstream of the shock.) Thus the radiative shock that is the subject of this work can be thought as being embedded in a usual hydrodynamical shock, a "shock within a shock" (Mihalas & Mihalas 1984), or a hydrodynamical shock as being a radiative shock with an infinitely or unresolved thin precursor. Separate test simulations with extremely high opacity values ($\kappa = 10^2\ {\rm cm^2\ g^{-1}}$), such that the precursor is contained in the simulation domain, confirm that the postshock entropy is higher than the entropy far from the shock.

The postshock entropies are respectively $S \approx 12$ and 20 k_B/baryon for the molecular and atomic cases. Compared to the range of entropies seen for cold starts to hot starts ($S \approx 8$–14 k_B/baryon; Marley et al. 2007; Spiegel & Burrows 2012; Mordasini 2013), this is an extremely large difference, which is due mostly to the different mean molecular weights. Moreover, it highlights the importance of using a self-consistent EOS that follows in particular the dissociation of hydrogen. However, the entropy values do not depend sensitively on the precise opacity (see Figure 2).

Finally, it is important to remember that these entropy values are meant to be rather indicative at this stage. First of all, they are not entirely self-consistent with the probable state of the hydrogen in all parts of the domain (see the phase diagram in Figure 2). Second, what they actually imply for the postformation entropy needs to be worked out separately, with a study of the postshock settling region and its coupling to the planet interior (Berardo et al. 2017; G.-D. Marleau et al. 2017, in preparation).

3.5. Luminosity

The luminosity increases from the imposed $L = 0$ value at $r_{\rm min}$ to the shock where it jumps by a finite amount ΔL, then decreasing with radius. The value of L downstream of the shock reflects in part the cooling of the layers below it, and it is set in reality also by (inefficient) convective energy transport, which we do not attempt to include in these simulations. Thus the postshock gas will probably have a different thermal history than if the layers were allowed to sink farther down into the planet instead of stopping at most at $r_{\rm min}$. Nevertheless, the obtained immediate postshock luminosities are roughly $L_{\rm downstr} \approx 3 \times 10^{-4}\, L_\odot$ and thus have values comparable to the (rough) internal luminosities of accreting planets (Mordasini et al. 2017). Therefore, the inclusion of convection or similar changes to the temperature structure should not lead to very different values for the postshock region.

A general feature of these shock simulations is that L decreases radially outward. This is not due to absorption of the light with optical depth according to $L \propto \exp(-\Delta\tau)$, as one might naively expect, but rather reflects energy conservation. To derive this, we start with the total energy equation (e.g., Kuiper et al. 2010)

$$\frac{dE_{\rm tot}}{dt} + \nabla \cdot ([E_{\rm kin} + H]v + F_{\rm rad}) = \rho v \cdot g, \tag{30}$$

where the total energy volume density is $E_{\rm tot} = E_{\rm kin} + H$, with $E_{\rm kin} = \frac{1}{2}\rho v^2$, and the enthalpy is $H = E_{\rm int} + P$. For a constant EOS, $E_{\rm int} = \rho c_{\rm v} T = \rho/(\gamma - 1) \times k_{\rm B}T/(\mu m_{\rm H}) = P/(\gamma - 1)$, where $c_{\rm v}$ is the heat capacity at a constant volume. It is easy to verify that the thermal timescales are much shorter than the dynamical timescales, so that the flow is in a steady state and the time derivative $dE_{\rm tot}/dt$ can be neglected. Also, $\dot{M}$ is constant radially. Remembering that $\nabla \cdot F = 1/r^2 d/dr\,(r^2 F)$ for a vector F, Equation (30) becomes

$$\frac{dL}{dr} = \dot{M}\frac{dh}{dr} + \dot{M}\frac{d}{dr}\left(\frac{1}{2}v^2 - \frac{GM_{\rm p}}{r}\right), \tag{31}$$

where $h = H/\rho$ is the specific enthalpy per mass and is $h = \gamma/(\gamma - 1)k_{\rm B}T/(\mu m_{\rm H})$ for a constant EOS. The accretion rate $\dot{M}$ was taken to be positive here, that is, $\dot{M} = |4\pi r^2 \rho v|$, and one can trivially replace $GM_{\rm p}/r$ by $GM_{\rm p}\,(1/r - 1/R_{\rm acc})$. If the second term on the right-hand side of Equation (31) is small, Equation (31) shows that the radial decrease in L is mostly due to the inward increase in enthalpy. Therefore, it is not an explicit function of the optical depth, although $T(r)$ and thus $h(T)$ are indirectly set by the opacity. Note that this derivation is valid for a general EOS (with variable effective γ) and also does not depend on the opacity being constant.

Equation (31) can be integrated to yield, when the second term on the right-hand side of Equation (31) is negligible,

$$L(r) - L_{\rm downstr} = \Delta L(r_{\rm shock})\left[1 - \frac{\dot{M}\Delta h(r)}{\Delta L(r_{\rm shock})}\right], \tag{32}$$

where $\Delta L(r_{\rm shock}) = \eta^{\rm kin} L_{\rm acc,max}$ is the jump in luminosity at the shock, and $\Delta h(r) \equiv h(r_{\rm shock}) - h(r)$ is the change in enthalpy relative to the shock, with $\Delta h > 0$ for outward-decreasing enthalpy. This result seems plausible: the inward enthalpy flux is comparable to the outward radiation flux only when the infalling gas absorbs a significant fraction of the radiation and thus decreases L. The maximal drop in luminosity occurs for $h(r_{\rm max}) \ll h(r_{\rm shock})$, that is, when the effective nebula temperature $T_{\rm neb} \ll T_{\rm shock}$. This leads to $L(r_{\rm max}) - L({r_{\rm shock}}^{+}) = -\dot{M}h(T_{\rm shock})$.

3.6. Efficiencies

Next we show in Figure 3 the main result for the examples of Figure 2, the loss efficiency $\eta^{\rm phys}$ of the accretion shock. We recall that $\eta^{\rm phys} = 0$ would correspond to all of the kinetic energy of the gas being absorbed by the planet and the gas being accreted, while $\eta^{\rm phys} = 100\%$ would correspond to the entire kinetic energy being radiated away when going out to the accretion radius $R_{\rm acc}$, roughly the Hill sphere (here approximated by the outer radius near $R_{\rm acc}$). Contrary to $\eta^{\rm kin}$, $\eta^{\rm phys}$ takes into account the energy recycling that occurs due to the incoming gas absorbing the radiation liberated at the shock (see Equation (18) and the discussion below Equation (20)). We find that they are $\eta^{\rm phys} \approx 85\%$ for the atomic hydrogen cases with different opacities, and $\eta^{\rm phys} \approx 95\%$ for the molecular case. Thus, a fraction $1 - \eta^{\rm phys} \approx 5\%$–$15\%$ of the total incoming energy is added to the planet. How significant this is for the energy budget of the planet can be assessed by comparing $(1 - \eta^{\rm phys})\dot{E}(r_{\rm max})$ to the internal luminosity of the planet. For these simulations, both are typically of the same order of magnitude, implying that the accreting gas is able to heat the downstream region. As mentioned above, how this then affects the entropy and luminosity of the planet and their evolution will have to be studied separately.

We show also the efficiencies from simulations covering a range of accretion rates $\dot{M} = 10^{-5}$–$10^{-2}\, M_\oplus\ {\rm yr}^{-1}$, masses $M_{\rm p} \approx 0.3$–$10\, M_{\rm J}$, and shock locations $r_{\rm shock} \approx 1$–$20\, R_{\rm J}$, and varying again the opacity. At the largest radii, efficiencies down to almost 20% are reached, and to 99% at the other extreme.

By contrast, the "kinetic efficiency" is $\eta^{\rm kin} \approx 100\%$ (up to the numerical accuracy of the code given the resolution) for all simulations shown in Figure 3, with $(1 - \eta^{\rm kin})E_{\rm tot}$ smaller by orders of magnitude than $L_{\rm p}$. In other words, the entire kinetic energy is converted to an immediate jump in the luminosity as the gas is brought to subsonic speeds through the shock. However, a significant fraction does get reabsorbed in the

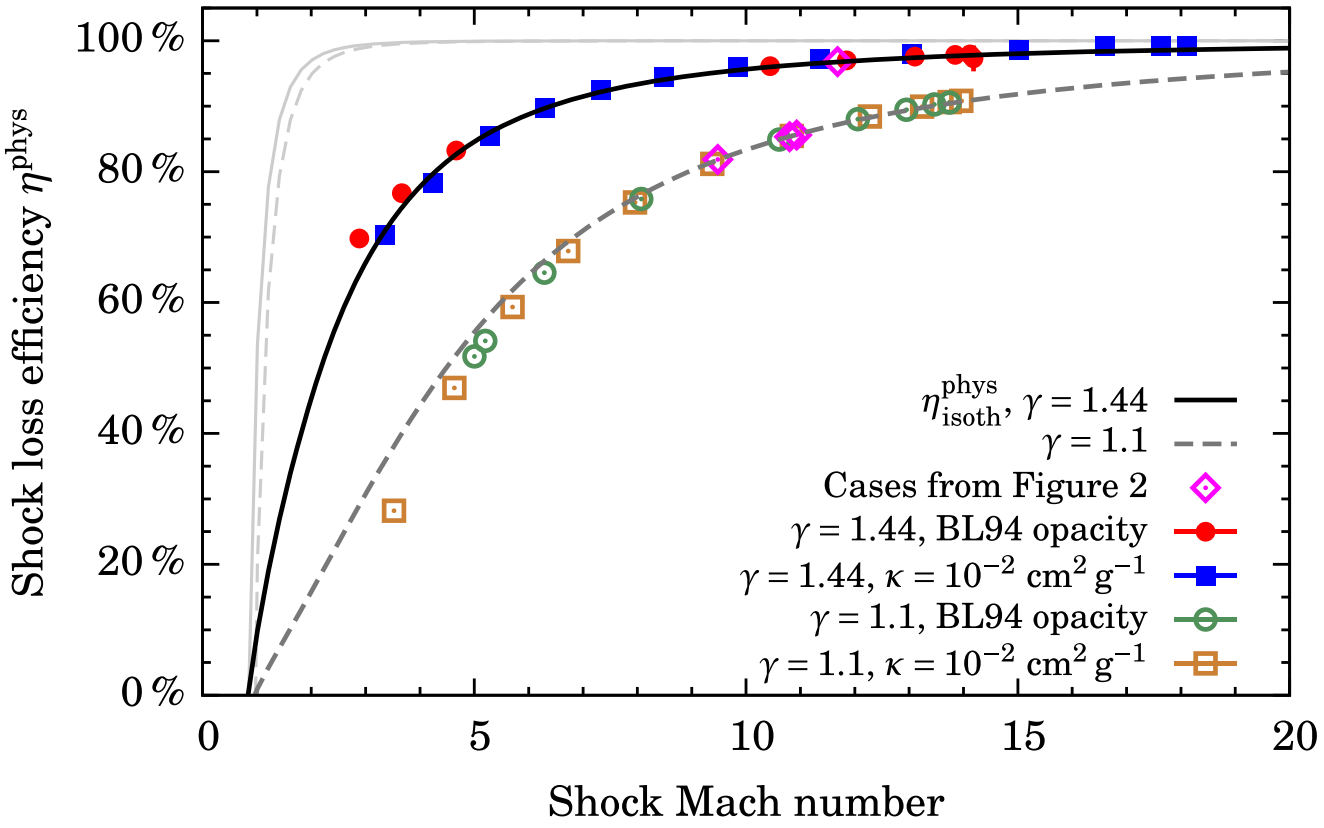

Figure 3. Physical loss efficiency $\eta^{\rm phys}$ of the radiative accretion shock (see Equation (18)). The limit $\eta^{\rm phys} = 0$ corresponds to all of the incoming energy being absorbed (no loss), while $\eta^{\rm phys} = 100\%$ means that the kinetic energy of the gas entirely leaves the accretion flow onto the planet; see Section 2.6.1. The diamonds display the efficiency for the cases shown in Figure 2. The other points come from considering a range of accretion rates $\dot{M} = 10^{-5}$–$10^{-2}\,M_\oplus\,{\rm yr}^{-1}$, masses $M_{\rm p} \approx 0.3$–$10\,M_{\rm J}$, and shock locations $r_{\rm shock} \approx 1$–$20\,R_{\rm J}$. Both constant and tabulated opacities are used as indicated in the legend. The last four groups of points (see the legend) all take $\mu = 2.353$. The results match the analytical result for an isothermal shock at the measured Mach number (Equation (36)) for $\gamma = 1.44$ and $\gamma = 1.1$ (solid black and dashed dark gray curves, respectively). Theoretical curves for the "kinetic efficiency" $\eta^{\rm kin}_{\rm isoth}$ for an isothermal shock (Equation (34) from Commerçon et al. 2011) are shown for reference (light gray curves).

accretion flow, leading to the lower $\eta^{\rm phys}$ values. Nevertheless, we find generally that the precursor is greater than the accretion radius, which is of order of the Hill radius. The optical depths from the shock to the Hill sphere are at most $\Delta\tau \sim 30$, and using a variable EOS (which would yield other temperatures) should not change this significantly. We therefore expect the radiation to always be able to escape from the shock to the local disk (the nebula).

These numerical results can be compared to analytical theory for radiative shocks. Drake (2006, his Equation (7.82)) derived that the kinetic efficiency of a shock in which radiation pressure is negligible is in general given by

$$\eta^{\rm kin} \equiv \frac{\Delta F}{\frac{1}{2}\rho_- v_-^3} = 1 + \frac{2}{(\gamma-1)\mathcal{M}^2}\frac{\mathfrak{r}-1}{\mathfrak{r}} + \frac{\gamma+1}{\gamma-1}\frac{1}{\mathfrak{r}^2}. \quad (33)$$

where $\Delta F = \Delta L/(4\pi r^2)$ is the jump in flux at the shock $\mathfrak{r} = \rho_2/\rho_1$ is the ratio of the postshock to the preshock density. For isothermal shocks (as we find here), $\mathfrak{r} = \gamma\mathcal{M}^2$, and Commerçon et al. (2011) show that the efficiency is then

$$\eta^{\rm kin}_{\rm isoth} = 1 - \frac{1}{\gamma^2\mathcal{M}^4}. \quad (34)$$

Thus a higher Mach number leads to a higher fraction of the incoming kinetic energy being converted to radiation for an isothermal shock. Since the total energy flux is

$$\rho v e_{\rm tot} = \rho v\left(\frac{1}{2}v^2 + h\right) \quad (35a)$$

$$= \frac{1}{2}\rho v^3\left(1 + \frac{2}{\gamma-1}\frac{1}{\mathcal{M}^2}\right), \quad (35b)$$

we can derive that the physical efficiency, as measured by ΔL at the shock, is

$$\eta^{\rm phys}_{\rm isoth} = \eta^{\rm kin}_{\rm isoth} \times \left(1 + \frac{2}{\gamma-1}\frac{1}{\mathcal{M}^2}\right)^{-1}. \quad (36)$$

Therefore, the physical efficiency is lower than the kinetic since the former considers the heating of the radiative precursor. In other words, not all radiation liberated at the shock can leave the planet, and therefore it gets incorporated in the planet's entropy. Note that naively one might expect in strongly supersonic flows ($\mathcal{M} = v/c_{\rm s} \gg 1$) the internal energy (measured by $c_{\rm s}^2$) to be negligible compared to the kinetic energy (measured by v^2), but the $2/(\gamma-1)$ factor can make this assumption cruder than expected, especially for low γ values; for instance, when $\gamma = 1.1$ and even with a high Mach number $\mathcal{M} = 10$, the factor $2/\mathcal{M}^2(\gamma-1)$ is 0.2, that is, a 20% contribution.

The Mach numbers are in the range $\mathcal{M} \approx 3$–20, and the $\eta^{\rm phys}_{\rm isoth}$ curve is compared to the data in Figure 3 for $\gamma = 1.1$ and $\gamma = 1.44$. The agreement is excellent. The deviation from the theoretical curve, seen for a few simulations, is possibly due to small measurement errors related to the identification of the shock region and to inaccuracies in the measurement of the velocity at which the shock is spreading; this speed becomes somewhat important (at the several-percent level) at low Mach numbers. However, the overall agreement is excellent, independent of the opacity and optical depth in the flow (not shown).

At least for the constant EOS used here, these simulations and other tests indicate that extreme parameter values (e.g., $\dot{M} > 10^{-1}\,M_\oplus\,{\rm yr}^{-1}$ or $\kappa > 100\,{\rm cm}^2\,{\rm g}^{-1}$) would be needed to obtain a shock with a Mach number $\mathcal{M} \lesssim 2$, in which $\eta^{\rm kin}$ would clearly be lower than 100%. Note that, while $v_{\rm ff} \propto \sqrt{M_{\rm p}}$, very small masses are not sufficient to obtain a lower Mach number since $\mathcal{M} \propto v_{\rm ff}/\sqrt{T}$ at lower masses, the temperature in the preshock region too is smaller, which does not let $\mathcal{M}$ get much lower than about 3.

4. Discussion and Summary

We have studied spherically symmetric gas accretion onto a gas giant during the detached runaway phase, when the gas falls freely from the accretion radius (of order of the Hill radius) onto the planet, where it shocks. We determine the radiative efficiency of the shock at the planet's surface and argue that this should be defined with the total incoming energy flux, that is, taking both the kinetic and the internal energy into account. Even if, at a Mach number $\mathcal{M} = 4$, an isothermal shock converts 100% of the incoming kinetic energy into radiation, only 77% (40%) for $\gamma = 1.44$ ($\gamma = 1.1$) ultimately escapes, with 23% (60%) absorbed by the infalling gas and therefore reaccreted to the system. This efficiency has direct observational consequences as it controls the amount of radiation that leaves the planet and is possibly observable. The efficiency is also important since the complementary fraction is carried through the shock into the settling region, where the gas is being incorporated into the planet. To the best of our knowledge, the energetics of the shock have not yet been studied in detail as we have done, yet they are thought to be key in determining the postformation thermal state of gas giants. As is well known, there are several orders of magnitude of difference in the resulting luminosity between the two extreme cases, hot and cold starts (Marley et al. 2007).

We have considered both constant and tabulated opacities (Bell & Lin 1994) but have used only a constant EOS to concentrate on the shock physics. Therefore, the numerical results are rather illustrative in a quantitative sense, but the qualitative behavior of the radial profiles and the derived results revealed a number of interesting features. We find the following.

1. The shock was observed always to be isothermal, which corresponds in the classical terminology to a supercritical shock (Stahler et al. 1980; Mihalas & Mihalas 1984).
2. The effective speed of light of the escaping photons is always much larger than the gas flow speed ($F_{\rm read}/E_{\rm rad} \gg v$), so that the upstream region is in the "static diffusion" regime (Mihalas & Mihalas 1984).
3. Our radiation-hydrodynamics simulations confirm, over a large range of Mach numbers, the theoretical expression for the efficiency given by Commerçon et al. (2011, our Equation (34)).
4. Unrealistically high constant opacity values were separately verified to be needed to cause the luminosity generated at the shock to be completely absorbed in the precursor, ahead of the shock region. For reasonable constant or tabulated opacities, all luminosity profiles are qualitatively similar, decreasing by some amount with increasing distance and with a nonzero value at the outer edge (see point 8 below). An analytical formula is derived for the drop based on energy conservation and shows that, roughly, the decrease in luminosity is significant only if the incoming gas carries a significant amount of energy compared to the accretion luminosity.
5. We generally find higher shock temperatures than predicted by the usual estimate of the shock temperature, Equation (28b). We show analytically that this is a lower bound. The shock temperature being higher is due to the radiation of the preshock matter. (The difference between the actual and estimated temperature can be large—nearly 1000 K in our examples—enough to possibly change the state of the gas significantly, from molecular to atomic.) This leads to lower Mach numbers and thus overall lower efficiencies of the shock.
6. The entropy was seen to decrease across the shock since it is in fact the radiative shock embedded in the hydrodynamical one; over the latter, the entropy does increase as expected. The decrease ΔS was found to be large, with $\Delta S \approx 1.5$–$4\ k_{\rm B}$/baryon for the examples considered. Thus the shock is very efficient in radiating away the entropy of the shocked gas. The postshock values were seen to be clearly high ($S > 12\ k_{\rm B}$/baryon), with the choice for the EOS making a significant difference. We however point out that the obtained densities and temperatures were not consistent with the assumed (constant) mean molecular weight and heat capacity. Therefore the entropy values, while consistent within the parameter choices for the simulations, should in general be expected to be different when using a nonconstant complete EOS. This will be a subject of Paper II.
7. For most of the formation parameter space, nearly all of the kinetic energy is radiated away at the shock, that is, $\eta^{\rm kin} \approx 100\%$. This is in agreement with the analytical formula of Drake (2006) and Commerçon et al. (2011), which predicts $\eta^{\rm kin} \approx 100\%$ for sufficiently high upstream Mach numbers ($\mathcal{M} \gtrsim 3$). However, it is important to remember that the Mach number itself depends on the shock temperature, which is an outcome of the simulations and can at best only be estimated beforehand.
8. However, most importantly, we found that the physical (or "planet-heating") efficiency is usually smaller than 100%, with values down to $\eta^{\rm phys} \approx 20\%$ for a reasonable range of parameter values. This energy flux coming into the planet is often comparable to or in fact much higher than its internal luminosity, suggesting that the accretion process can also play an important role energetically. The complementary fraction of the accretion luminosity should reach at least the Hill sphere and may even have already been detected for a few low-mass objects in the

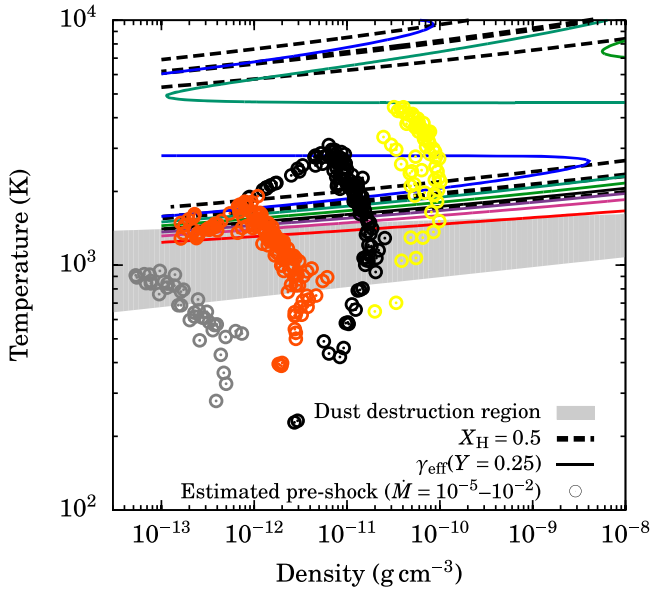

Figure 4. Estimate of the shock temperature and upstream density made by assuming $\eta^{kin} = 1$ (an isothermal shock), $f_{red} = 1$ upstream, and $L(r_{shock}^-) \ll L(r_{shock}^+)$, which leads to $4\pi R_p^2 caT_{shock}^4 \approx GM_p\dot{M}/R_p$, with ρ given by the free-fall density (Equations (28b) and (12), respectively). Shown are contours of $\gamma = 1.10$–1.40 in steps of 0.05 (blue through green to red) with $\gamma \approx 1.4$ from ≈100 to 1000 K, as well as of the ionization or dissociation fraction for hydrogen of $X_H = 0.1$, 0.5, and 0.9 (black dashed lines), and the region of dust destruction in Bell & Lin (1994) (gray band), with κ of order 1 cm^2 g^{-1} at lower temperatures. The groups of points are, from left to right, for $\log \dot{M}/(M_\oplus\ \mathrm{yr}^{-1}) = -5, -4, -3$, and -2.

form of Hα emission (Close et al. 2014; Quanz et al. 2015; Sallum et al. 2015).

The next steps will be to extend our analysis to cases of a nonconstant EOS to obtain realistic values for the efficiencies, and to verify the assumption of perfect gas–radiation coupling (the 1-T assumption) with 2-T radiation transport calculations. Then, we will couple these efficiency results to formation calculations, especially in the framework of population synthesis, to make predictions of the postformation luminosity of gas giants.

Beyond this, due to the generality of our approach, we can easily perform these shock calculations not only in the context of core accretion but also for other accretion scenarios. Indeed, these calculations apply also to magnetospheric accretion (Koenigl 1991; Lovelace et al. 2011), where high-density accretion columns hit the surface of the star; a similar accretion geometry is a possibility in the context of planet formation (Katarzyński et al. 2016; G.-D. Marleau et al. 2017, in preparation). Also we could easily adapt the parameters (mass, shock radius) to values appropriate for the flow geometry revealed by global three-dimensional simulations (D'Angelo et al. 2003; Tanigawa et al. 2012; Szulágyi et al. 2016; Szulágyi & Mordasini 2017), where gas falls from high latitudes and shocks on the circumplanetary disk.

The authors acknowledge the valuable support of Th. Henning for this project. This work has benefited greatly from discussions with P. Mollière, and we thank also the referee, G. Chabrier, as well as A. Cumming, N. Turner, W. Benz, W. Kley, M. Ikoma, and R. Pudritz for discussions and insightful comments. K.-M. Dittkrist, M. Schulik, S. Ataiee, and A. Emsenhuber are also thanked for useful conversations. The simulations presented here were performed on the `ba(t)chelor` cluster at the MPIA. G.-D.M. gratefully acknowledges a research fellowship of the International Max-Planck Research School for Astronomy and Cosmic Physics in Heidelberg (IMPRS-HD). G.-D.M. and C.M. acknowledge support from the Swiss National Science Foundation under grant BSSGI0_155816 "PlanetsInTime." Parts of this work have been carried out within the frame of the National Centre for Competence in Research PlanetS supported by the SNSF. R.K. acknowledges financial support within the Emmy Noether research group on "Accretion Flows and Feedback in Realistic Models of Massive Star Formation" funded by the German Research Foundation under grant No. KU 2849/3-1.

Appendix
Relevant Parameter Space

Here we estimate the temperature and density values relevant for the shock by using the M_p, R_p, $\dot{M}$, and L_p values from the population synthesis of Mordasini et al. (2012a, 2012b). (These data and many more are available on the Data Analysis Centre for Exoplanets platform at https://dace.unige.ch/evolution/index.) Figure 4 shows the lower bound to the shock temperature for an isothermal shock (Equation (28b)) using the free-fall velocity, and the preshock density, given by Equations (11-12). We consider $M_p \approx 0.2$–$30\ M_J$ and $\dot{M} \approx 10^{-4}$–$10^{-2}\ M_\oplus\ \mathrm{yr}^{-1}$, with $r_{shock} \approx 1$–$30\ R_J$. Comparing to the contours of constant γ and the rough ρ–T region were dust is destroyed and the opacity drops from ~ 1 to $\sim 10^{-2}$ cm^2 g^{-1}, one can expect for $\dot{M} \lesssim 10^{-5}\ M_\oplus\ \mathrm{yr}^{-1}$ the hydrogen to remain molecular and dust to be only partially destroyed. At higher accretion rates, however, that is, for most of the parameter space of interest here, both dissociation and dust destruction are expected to play a role.

References

Arras, P., & Bildsten, L. 2006, ApJ, 650, 394
Ayliffe, B. A., & Bate, M. R. 2009, MNRAS, 393, 49
Baraffe, I., Vorobyov, E., & Chabrier, G. 2012, ApJ, 756, 118
Bell, K. R., & Lin, D. N. C. 1994, ApJ, 427, 987
Berardo, D., Cumming, A., & Marleau, G.-D. 2017, ApJ, 834, 149
Beuzit, J.-L., Fledt, M., Dohlen, K., et al. 2008, Proc. SPIE, 7014, 701418
Biller, B. A., Liu, M. C., Wahhaj, Z., et al. 2013, ApJ, 777, 160
Bodenheimer, P., Hubickyj, O., & Lissauer, J. J. 2000, Icar, 143, 2
Bowler, B. P. 2016, PASP, 128, 968
Brandt, T. D., McElwain, M. W., Turner, E. L., et al. 2014, ApJ, 794, 159
Chauvin, G., Lagrange, A.-M., Dumas, C., et al. 2004, A&A, 425, L29
Clanton, C., & Gaudi, B. S. 2016, ApJ, 819, 125
Close, L. M., Follette, K. B., Males, J. R., et al. 2014, ApJL, 781, L30
Commerçon, B., Audit, E., Chabrier, G., & Chièze, J.-P. 2011, A&A, 530, A13
D'Angelo, G., & Bodenheimer, P. 2013, ApJ, 778, 77
D'Angelo, G., Kley, W., & Henning, T. 2003, ApJ, 586, 540
Drake, R. P. 2006, High-Energy-Density Physics: Fundamentals, Inertial Fusion, and Experimental Astrophysics (Berlin: Springer)
Drake, R. P. 2007, PhPl, 14, 043301
Ensman, L. 1994, ApJ, 424, 275
Freedman, R. S., Marley, M. S., & Lodders, K. 2008, ApJS, 174, 504
Fung, J., Artymowicz, P., & Wu, Y. 2015, ApJ, 811, 101
Hartmann, L., Cassen, P., & Kenyon, S. J. 1997, ApJ, 475, 770
Katarzyński, K., Gawroński, M., & Goździewski, K. 2016, MNRAS, 461, 929
Keith, S. L., & Wardle, M. 2015, MNRAS, 451, 1104
Koenigl, A. 1991, ApJL, 370, L39
Kuiper, R., Klahr, H., Dullemond, C., Kley, W., & Henning, T. 2010, A&A, 511, A81
Kuiper, R., & Klessen, R. S. 2013, A&A, 555, A7
Lafrenière, D., Jayawardhana, R., & van Kerkwijk, M. H. 2008, ApJL, 689, L153
Lagrange, A.-M., Gratadour, D., Chauvin, G., et al. 2009, A&A, 493, L21
LeBlanc, J. M., & Wilson, J. R. 1970, ApJ, 161, 541
Levermore, C. D. 1984, JQSRT, 31, 149

Levermore, C. D., & Pomraning, G. C. 1981, ApJ, 248, 321
Lissauer, J. J., Hubickyj, O., D'Angelo, G., & Bodenheimer, P. 2009, Icar, 199, 338
Lovelace, R. V. E., Covey, K. R., & Lloyd, J. P. 2011, AJ, 141, 51
Macintosh, B., Graham, J. R., Ingraham, P., et al. 2014, PNAS, 111, 12661
Malygin, M. G., Kuiper, R., Klahr, H., Dullemond, C. P., & Henning, T. 2014, A&A, 568, A91
Marleau, G.-D., & Cumming, A. 2014, MNRAS, 437, 1378
Marley, M. S., Fortney, J. J., Hubickyj, O., Bodenheimer, P., & Lissauer, J. J. 2007, ApJ, 655, 541
Marois, C., Macintosh, B., Barman, T., et al. 2008, Sci, 322, 1348
Mignone, A., Bodo, G., Massaglia, S., et al. 2007, ApJS, 170, 228
Mignone, A., Zanni, C., Tzeferacos, P., et al. 2012, ApJS, 198, 7
Mihalas, D., & Mihalas, B. W. 1984, Foundations of Radiation Hydrodynamics (Oxford: Oxford Univ. Press)
Mizuno, H. 1980, PThPh, 64, 544
Mordasini, C. 2013, A&A, 558, A113
Mordasini, C., Alibert, Y., Klahr, H., & Henning, T. 2012a, A&A, 547, A111
Mordasini, C., Alibert, Y., Georgy, C., et al. 2012b, A&A, 547, A112
Mordasini, C., Marleau, G.-D., & Mollière, P. 2017, A&A, submitted
Oppenheimer, B. R., Beichman, C., Brenner, D., et al. 2012, Proc. SPIE, 8447, 20
Ormel, C. W., Shi, J.-M., & Kuiper, R. 2015, MNRAS, 447, 3512
Paxton, B., Cantiello, M., Arras, P., et al. 2013, ApJS, 208, 4
Peters-Limbach, M. A., Groff, T. D., Kasdin, N. J., et al. 2013, Proc. SPIE, 8864, 88641
Pollack, J. B., Hollenbach, D., Beckwith, S., et al. 1994, ApJ, 421, 615
Quanz, S. P., Amara, A., Meyer, M. R., et al. 2015, ApJ, 807, 64
Sallum, S., Follette, K. B., Eisner, J. A., et al. 2015, Natur, 527, 342
Semenov, D., Henning, T., Helling, C., Ilgner, M., & Sedlmayr, E. 2003, A&A, 410, 611
Skemer, A. J., Hinz, P., Esposito, S., et al. 2014, Proc. SPIE, 9148, 91480
Spiegel, D. S., & Burrows, A. 2012, ApJ, 745, 174
Stahler, S. W., Shu, F. H., & Taam, R. E. 1980, ApJ, 241, 637
Szulágyi, J., Masset, F., Lega, E., et al. 2016, MNRAS, 460, 2853
Szulágyi, J., & Mordasini, C. 2017, MNRAS, 465, L64
Tanigawa, T., Ohtsuki, K., & Machida, M. N. 2012, ApJ, 747, 47
Uribe, A. L., Klahr, H., & Henning, T. 2013, ApJ, 769, 97
Vaytet, N., Chabrier, G., Audit, E., et al. 2013a, A&A, 557, A90
Vaytet, N., González, M., Audit, E., & Chabrier, G. 2013b, JQSRT, 125, 105
Zel'dovich, Y. B., & Raizer, Y. P. 1967, Physics of Shock Waves and High-temperature Hydrodynamic Phenomena (New York: Academic)
Zhu, Z. 2015, ApJ, 799, 16